

## Journal Name

Crossmark

PAPER

RECEIVED  
dd Month yyyyREVISED  
dd Month yyyy

# Likelihood-Based One-Class Scoring in CWT Latent Space for Confusion-Limited LISA Gravitational-Wave Detection

Jericho Cain<sup>1,\*</sup> <sup>1</sup>Physics Department, Portland Community College, Portland, OR, USA

\*Author to whom any correspondence should be addressed.

**E-mail:** jericho.cain@gmail.com**Keywords:** gravitational waves, LISA, one-class anomaly detection, latent density estimation, continuous wavelet transform, source separation

## Abstract

We study one-class scoring for resolvable-source detection in confusion-limited LISA time-series data represented as continuous-wavelet-transform (CWT) scalograms. With data generation and preprocessing held fixed, we benchmark geometry-style scoring against likelihood-style latent-density scoring, while also evaluating morphology-augmented and contrastive variants. Geometry-only and geometry+morphology methods provide modest gains over the reconstruction baseline, and contrastive variants do not show stable improvement. Likelihood scoring on AE latents is consistently stronger: across three seeds, latent-only likelihood reaches ROC-AUC  $0.8555 \pm 0.0181$  and PR-AUC  $0.9219 \pm 0.0118$ , versus ROC-AUC  $0.7663 \pm 0.0450$  and PR-AUC  $0.8667 \pm 0.0255$  for AE+manifold. These results indicate that explicit latent density modeling can outperform local off-manifold distance in this confusion-limited regime. We provide seed-based comparisons, unified ROC/PR visual summaries, and reproducible experimental artifacts to support follow-on work in LISA anomaly detection.

## 1 Introduction

The mHz gravitational-wave band targeted by LISA is expected to be crowded with Galactic compact binaries, especially double white dwarfs. At low frequencies, many of these systems are unresolved and form a confusion-limited foreground; at higher frequencies or amplitudes, a smaller subset becomes individually resolvable [1, 2]. This foreground is scientifically valuable in its own right, but it is also a practical obstacle: unresolved structure can hide or distort weaker sources [3].

Foreground modeling and source-separation strategy are therefore not optional implementation details; they define the detection setting itself. Earlier studies showed that identifying and subtracting bright systems can materially change residual background statistics and therefore the effective detection landscape [2, 3]. Sensitivity-curve assumptions and mission-level requirements add another layer of realism to this problem [4, 5].

In this paper we focus on one-class scoring in latent feature space, motivated by the regime where anomalies are rare, diverse, or poorly labeled. Instead of training a closed-set classifier, we model the dominant background class and rank candidates by how atypical they are. The core question is deliberately narrow: with data generation and preprocessing held fixed, which scoring family better separates resolvable sources from the confusion background?

We compare two approaches that are often discussed together but seldom isolated in a controlled benchmark: local geometric deviation in latent space (manifold-style scoring) and explicit latent density modeling (likelihood-style scoring). Geometry-based scores are intuitive for autoencoder embeddings, but dense foreground structure can make local distance less reliable than expected. Likelihood methods can better capture global background structure, though they introduce their own modeling choices. By evaluating these approaches under a frozen protocol and across multiple seeds, we show that likelihood-based latent scoring is the more robust choice in this setting, and we provide reproducible artifacts to support follow-up methodological work.

## 2 Related Work

Classical gravitational-wave searches were built around two strong ideas: matched filtering for modeled sources, and coherent burst methods for less-modeled transients. Template placement theory remains the backbone of compact-binary searches [6]. In parallel, multiresolution and coherent burst pipelines established a robust time–frequency route for non-template analyses [7, 8].

The LISA setting raises a different challenge. In the milli-Hz band, unresolved Galactic binaries are expected to produce a confusion foreground over a nontrivial frequency range [1, 2]. That foreground is not a side issue; it is part of the operating environment for source characterization [3]. Mission and sensitivity studies reinforce this framing, both in instrument-level requirements and in practical sensitivity construction [9, 5]. Updated sensitivity-curve treatments make the same point in analysis form [10, 4].

Machine learning has already shown value in gravitational-wave pipelines. Deep models have been used for fast detection and parameter-estimation-adjacent tasks in ground-based data [11, 12]. Other work has focused on detector-noise structure and data-quality classification [13]. There are also modern examples of unsupervised or source-agnostic strategies, including recurrent autoencoder approaches and newer anomaly-detection studies [14, 15]. These results are promising, but most papers evaluate one family at a time.

Our recent papers are the direct lead-in. [16] showed that CWT-based autoencoder representations can support template-free scoring in realistic LIGO conditions. [17] then adapted that representation logic to confusion-limited source-separation experiments with latent geometry scoring. What remained unclear was whether geometry-based distance is actually the best one-class scoring rule in this regime.

That question has a clear precedent in the anomaly-detection literature. One branch focuses on support estimation and one-class decision boundaries [18]. Another branch models density explicitly, typically with mixture models fitted by EM or with nonparametric estimators [19, 20]. In gravitational-wave analyses, these branches are usually evaluated in different data setups, with different preprocessing and operating assumptions, making direct comparison difficult.

This paper targets that gap directly. We hold data construction, CWT representation, and evaluation protocol fixed, and isolate only the scoring rule, enabling a like-for-like comparison between geometry-style and likelihood-style one-class scoring in the LISA confusion-limited regime.

## 3 Data and Experimental Protocol

### 3.1 Synthetic benchmark design

This study uses a controlled synthetic benchmark to compare one-class scoring strategies in a confusion-limited LISA setting. The goal is not to claim full mission realism; it is to hold data generation fixed so method-level effects are measurable. The design follows the confusion-background framing used in prior LISA studies [1, 2, 3] and is aligned with mission-level sensitivity context [4, 5].

All segments are generated in the time domain with duration  $T = 3600$  s and sampling rate  $f_s = 1$  Hz, yielding 3600 samples per segment.

### 3.2 Instrumental noise model

Instrumental noise is synthesized in frequency space from an analytic one-sided PSD with acceleration and optical metrology terms. We define

$$S_{\text{acc}}(f) = (3 \times 10^{-15})^2 \left( 1 + \left( \frac{4 \times 10^{-4}}{f} \right)^2 \right) \left( 1 + \left( \frac{f}{8 \times 10^{-3}} \right)^4 \right), \quad (1)$$

$$S_{\text{oms}}(f) = (15 \times 10^{-12})^2, \quad (2)$$

and combine them as

$$S_n(f) = \frac{10}{3L^2} \left[ S_{\text{oms}}(f) + \frac{(3 + \cos(2f/f_*))S_{\text{acc}}(f)}{(2\pi f)^2} \right], \quad (3)$$

with  $L = 2.5 \times 10^9$  m and  $f_* = 19.09$  mHz.

For a segment of duration  $T$ , we generate complex Gaussian frequency-domain samples and color them by

$$\tilde{n}(f_k) = (a_k + ib_k) \sqrt{\frac{S_n(f_k)}{2\Delta f}}, \quad a_k, b_k \sim \mathcal{N}(0, 1), \quad (4)$$

then apply inverse real FFT to obtain  $n(t)$ . PSD values are interpolated onto segment FFT bins before coloring.

### 3.3 Waveform models and parameter draws

Waveforms are generated analytically. We use three source classes.

For MBHB, the implementation uses a PN-inspired chirp with

$$f(t) = f_{\text{start}} \left( 1 - \frac{|t - t_c|}{\tau} \right)^{-3/8}, \quad \tau = \frac{5c^5}{256(\pi f_{\text{start}})^{8/3}(GM_c)^{5/3}}, \quad (5)$$

for pre-merger times, phase from cumulative frequency integration, and inclination-dependent plus/cross projection. Random draws use:  $m_1 \in [10^4, 10^7]M_\odot$ ,  $q = m_2/m_1 \in [0.1, 1]$ ,  $d_L \in [1, 20]$  Gpc,  $f_{\text{start}} \in [10^{-4}, 10^{-2}]$  Hz.

For EMRI, we start from quasi-circular orbital frequency at radius  $r = pr_g$ ,  $r_g = GM/c^2$ :

$$f_{\text{orb}} = \frac{1}{2\pi} \sqrt{\frac{GM}{r^3}}, \quad f_{\text{gw}} = 2f_{\text{orb}}, \quad (6)$$

and use a leading-order radiation-reaction chirp term

$$\dot{f} \propto (\pi f_{\text{gw}})^{11/3} \left( \frac{GM}{c^3} \right)^{5/3} \frac{\mu}{M}. \quad (7)$$

The time series is built as a finite harmonic sum ( $n = 1, \dots, 5$ ) with eccentricity-weighted terms. Random draws use:  $M \in [10^5, 10^7]M_\odot$ ,  $\mu \in [1, 100]M_\odot$ ,  $p \in [6, 20]$ ,  $e \in [0, 0.5]$ ,  $d_L \in [0.5, 10]$  Gpc.

For Galactic binaries, we use a slowly chirping monochromatic model

$$f(t) = f_0 + \dot{f}t, \quad \phi(t) = 2\pi \left( f_0t + \frac{1}{2}\dot{f}t^2 \right) + \phi_0, \quad (8)$$

with inclination-projected plus/cross components. Random draws use  $f_0 \in [10^{-4}, 10^{-2}]$  Hz,  $A \in [10^{-22}, 10^{-20}]$ ,  $\dot{f} \in [-10^{-14}, 10^{-15}]$  Hz/s.

### 3.4 Confusion and resolvable-source construction

Background segments are defined as

$$x_{\text{bg}}(t) = n(t) + \sum_{j=1}^{N_c} h_{\text{GB}}^{(j)}(t), \quad (9)$$

where each confusion component is a weak Galactic-binary waveform rescaled to target SNR drawn uniformly from a confusion interval. In the main run we set  $N_c = 1000$  and confusion SNR range  $[0.1, 2.0]$ .

SNR is computed against the same PSD by

$$\text{SNR}^2 = 4 \sum_k \frac{|\tilde{h}(f_k)|^2}{S_n(f_k)} \Delta f, \quad (10)$$

and each waveform is amplitude-scaled by  $\text{SNR}_{\text{target}}/\text{SNR}_{\text{current}}$ .

Positive test segments are built by adding one resolvable source:

$$x_{\text{sig}}(t) = x_{\text{bg}}(t) + h_{\text{res}}(t), \quad (11)$$

with  $\text{SNR}_{\text{target}} \sim \mathcal{U}(10, 50)$ . Labels are binary: background-only ( $y = 0$ ) and background+resolvable ( $y = 1$ ).

### 3.5 Dataset composition and reproducibility

For the benchmark configuration, we generate 5000 training background segments, 200 test background segments, and 400 test signal segments. Signal-type fractions are MBHB 50%, EMRI 30%, and bright Galactic binary 20%.

Seeded generation is deterministic at segment level (base seed plus index offsets), and per-segment metadata (source type, sampled parameters, and target SNR) are saved with the HDF5 datasets. This allows exact regeneration and audit of train/test composition.

### 3.6 Experimental protocol

All method comparisons use the same fixed synthetic dataset definition, preprocessing pipeline, and train/test split policy. For any head-to-head comparison, we do not change data-generation settings between methods; only the scoring formulation is changed.

To assess robustness to training stochasticity, we repeat each reportable method across three independent training seeds. These seed replicates use identical data protocol and evaluation procedure, so seed effects reflect optimization variability rather than data drift.

Model selection is performed with a validation-driven protocol that is held constant across methods. Final performance is reported on the same held-out test set for all methods.

Primary comparisons are based on ranking metrics computed from full test-score distributions. For seed-robustness reporting, we present aggregate statistics across the three runs (mean and standard deviation), alongside per-seed values in supplementary material.

## 4 Methods

We compare four scoring strategies under one fixed data protocol and one fixed CWT representation. The purpose of this section is to separate *representation* from *decision rule*: all methods consume the same preprocessed segments, but they define anomaly score in different ways. This lets us ask a narrow question: in a confusion-limited setting, which one-class scoring rule gives the best ranking of background-only versus background-plus-resolvable segments?

**Table 1.** Method summary with score definitions under the fixed protocol.

Method	Score definition	One-class model
AE+Manifold	$s_{\text{base}} = \alpha e_{\text{AE}} + \beta d_{\mathcal{M}}$	Latent local geometry
AE+Manifold+Morph	$s_{\text{fuse}} = (1 - \lambda)s_{\text{base}} + \lambda d_{\phi}$	Geometry + morphology kNN
Likelihood (Latent)	$s_{\text{lik}} = -\log p(f_{\theta}(x))$	GMM or KDE on latent
Likelihood (Morph+Latent)	$s = -\log p([\phi(x), f_{\theta}(x)])$	KDE on fused feature vector

### 4.1 Baseline Geometry Framework

This baseline geometry formulation and its confusion-limited motivation were introduced in our prior study [17]. The baseline model is an autoencoder trained only on background segments. Let  $x$  denote a CWT input and  $z = f_{\theta}(x)$  its latent code. The decoder  $g_{\theta}$  reconstructs  $\hat{x} = g_{\theta}(z)$ , and reconstruction error is

$$e_{\text{AE}}(x) = \|x - \hat{x}\|_2^2. \quad (12)$$

A latent manifold is then estimated from background latents using a local  $k$ -nearest-neighbor construction. For a test latent  $z$ , we compute a local off-manifold deviation  $d_{\mathcal{M}}(z)$ , interpreted as distance from typical background geometry.

The baseline anomaly score is

$$s_{\text{base}}(x) = \alpha e_{\text{AE}}(x) + \beta d_{\mathcal{M}}(f_{\theta}(x)), \quad (13)$$

with  $\alpha, \beta \geq 0$ . Operationally,  $e_{\text{AE}}$  captures reconstruction mismatch, while  $d_{\mathcal{M}}$  captures latent geometric novelty relative to background structure.

### 4.2 Physics-Feature Augmentation

We next add morphology descriptors computed from the same CWT inputs. These features summarize physically relevant time-frequency structure (track continuity, concentration, anisotropy, and related shape cues) that can be weakly expressed in raw latent distance alone.

From background morphology vectors  $\phi(x)$ , we build a one-class reference set and score each test sample by local neighbor distance in morphology space:

$$d_{\phi}(x) = \frac{1}{k} \sum_{j=1}^k \|\phi(x) - \phi_j^{(\text{bg})}\|_2. \quad (14)$$

A fused score is then defined by

$$s_{\text{fuse}}(x) = (1 - \lambda) s_{\text{base}}(x) + \lambda d_{\phi}(x), \quad \lambda \in [0, 1]. \quad (15)$$

This tests whether explicit morphology contributes information beyond latent geometry and reconstruction alone.

#### 4.3 Contrastive Geometry Exploration (Negative Result)

We also tested a contrastive encoder trained to pull augmented views of the same background segment together while pushing different segments apart. The intent was to sharpen latent neighborhoods before one-class scoring.

Given two stochastic augmentations  $t_1(x), t_2(x)$ , the encoder  $h_\psi$  is trained with an InfoNCE-style objective

$$\mathcal{L}_{\text{con}} = -\log \frac{\exp(\text{sim}(h_\psi(t_1(x_i)), h_\psi(t_2(x_i)))/\tau)}{\sum_j \exp(\text{sim}(h_\psi(t_1(x_i)), h_\psi(t_2(x_j)))/\tau)}, \quad (16)$$

with cosine similarity  $\text{sim}(\cdot, \cdot)$  and temperature  $\tau$ .

In our experiments this route did not produce stable gains over the autoencoder latent baseline. The negative result is retained because it is informative: stronger invariance pressure did not translate into better one-class separation in this confusion regime, despite lower training loss.

#### 4.4 Likelihood One-Class Scoring in Latent Space

The final method replaces distance-to-manifold scoring with explicit density modeling in latent space. Using background latents  $z \sim p_{\text{bg}}(z)$ , we fit one-class likelihood models and score by negative log-likelihood.

For Gaussian mixtures,

$$p_{\text{GMM}}(z) = \sum_{m=1}^M \pi_m \mathcal{N}(z | \mu_m, \Sigma_m), \quad (17)$$

with parameters estimated by EM [19]. For kernel density estimation,

$$p_{\text{KDE}}(z) = \frac{1}{Nh^d} \sum_{i=1}^N K\left(\frac{z - z_i}{h}\right), \quad (18)$$

following the nonparametric estimator in [20].

The anomaly score is

$$s_{\text{lik}}(x) = -\log p(f_\theta(x)), \quad (19)$$

where  $p$  is either  $p_{\text{GMM}}$  or  $p_{\text{KDE}}$ . Conceptually, this method asks a different question than manifold distance: not “how far from local geometry,” but “how probable under the background latent distribution.” This distinction is central to the comparison in Section 5.

## 5 Results

### 5.1 Performance Metrics

We report two threshold-free ranking metrics as primary results:

- ROC-AUC: area under the receiver operating characteristic, i.e., true-positive rate versus false-positive rate as threshold varies.
- PR-AUC (AP): area under the precision-recall curve, implemented as average precision (AP).

We also report single-threshold precision and recall. In this study, the decision threshold is the median anomaly score on the evaluation set, applied per method/seed:

$$\hat{y} = \mathbf{1}\{s(x) > \text{median}(s)\}.$$

This is the same rule used across baseline, fusion, and likelihood evaluations. Accordingly, precision/recall here should be read as protocol-dependent operating-point diagnostics, while ROC-AUC and PR-AUC/AP remain the main comparison metrics.

### 5.2 Primary Performance Comparison

Figure 1 shows representative single-run ROC and PR curves for the main methods. Table 2 reports 3-seed aggregates (mean  $\pm$  std) for the primary comparisons, with morphology-only shown as a single-run diagnostic.

**Table 2.** Primary performance comparison under fixed-config reporting. Values are mean  $\pm$  std over seeds 101/202/303. PR-AUC is reported as average precision (AP). Precision and recall use the fixed median-score decision rule. Fixed settings: baseline/fusion use  $\alpha = 0.5, \beta = 2.0$ ; fusion uses  $\lambda = 0.2$ ; latent likelihood uses GMM(48); morph+latent likelihood uses KDE( $h = 1.0$ ); morph-only uses kNN( $k = 8$ ).

Method	ROC-AUC	PR-AUC (AP)	Precision	Recall
AE+Manifold	$0.7663 \pm 0.0450$	$0.8667 \pm 0.0255$	$0.8411 \pm 0.0269$	$0.6308 \pm 0.0202$
AE+Manifold+Morph	$0.7688 \pm 0.0419$	$0.8716 \pm 0.0223$	$0.8389 \pm 0.0252$	$0.6292 \pm 0.0189$
<b>Likelihood (Latent)</b>	<b><math>0.8555 \pm 0.0181</math></b>	<b><math>0.9219 \pm 0.0118</math></b>	<b><math>0.8967 \pm 0.0167</math></b>	<b><math>0.6725 \pm 0.0125</math></b>
Likelihood (Morph+Latent)	$0.8033 \pm 0.0159$	$0.8836 \pm 0.0109$	$0.8489 \pm 0.0107$	$0.6367 \pm 0.0080$
Morph kNN	$0.6947 \pm 0.0000$	$0.8388 \pm 0.0000$	$0.7667 \pm 0.0000$	$0.5750 \pm 0.0000$

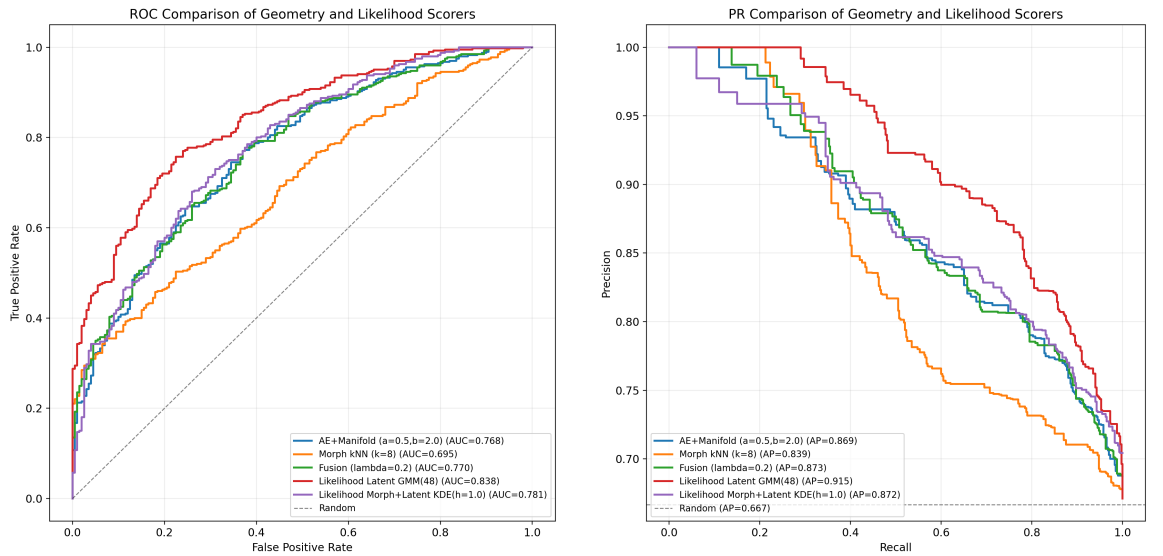


**Figure 1.** Representative single-run ranking curves across methods. Left: ROC (TPR vs FPR). Right: precision-recall. Legend values correspond to threshold-free summary scores for that run.

### 5.3 Likelihood Hyperparameter Ablation

We include a focused ablation on the latent-likelihood method (Table 3). For GMM scoring, performance improves with mixture complexity and peaks at  $k = 48$  in both ROC-AUC and PR-AUC. For KDE, bandwidth  $h = 1.0$  performs best in this regime; smaller bandwidths degrade ranking quality substantially. Figure 2 summarizes the latent-likelihood hyperparameter ablation for GMM components and KDE bandwidth.

**Table 3.** Latent-likelihood ablation on hyperparameters (mean  $\pm$  std over 3 seeds).

Setting	ROC-AUC	PR-AUC (AP)
<i>GMM components</i>		
$k = 1$	$0.7168 \pm 0.0200$	$0.8461 \pm 0.0127$
$k = 2$	$0.7162 \pm 0.0145$	$0.8527 \pm 0.0106$
$k = 4$	$0.7302 \pm 0.0087$	$0.8597 \pm 0.0058$
$k = 8$	$0.7559 \pm 0.0304$	$0.8738 \pm 0.0166$
$k = 16$	$0.8001 \pm 0.0228$	$0.8918 \pm 0.0070$
$k = 32$	$0.8435 \pm 0.0127$	$0.9205 \pm 0.0039$
$k = 48$	<b><math>0.8555 \pm 0.0181</math></b>	<b><math>0.9219 \pm 0.0118</math></b>
$k = 64$	$0.8543 \pm 0.0167$	$0.9197 \pm 0.0128$
$k = 96$	$0.8060 \pm 0.0390$	$0.8939 \pm 0.0265$
$k = 128$	$0.7743 \pm 0.0560$	$0.8632 \pm 0.0462$
<i>KDE bandwidth</i>		
$h = 0.05$	$0.6571 \pm 0.0109$	$0.8197 \pm 0.0112$
$h = 0.1$	$0.6286 \pm 0.0183$	$0.8056 \pm 0.0115$
$h = 0.2$	$0.6327 \pm 0.0233$	$0.8076 \pm 0.0187$
$h = 0.5$	$0.7499 \pm 0.0079$	$0.8435 \pm 0.0053$
$h = 1.0$	<b><math>0.8246 \pm 0.0208</math></b>	<b><math>0.8991 \pm 0.0143</math></b>
$h = 2.0$	$0.7037 \pm 0.0217$	$0.8421 \pm 0.0123$

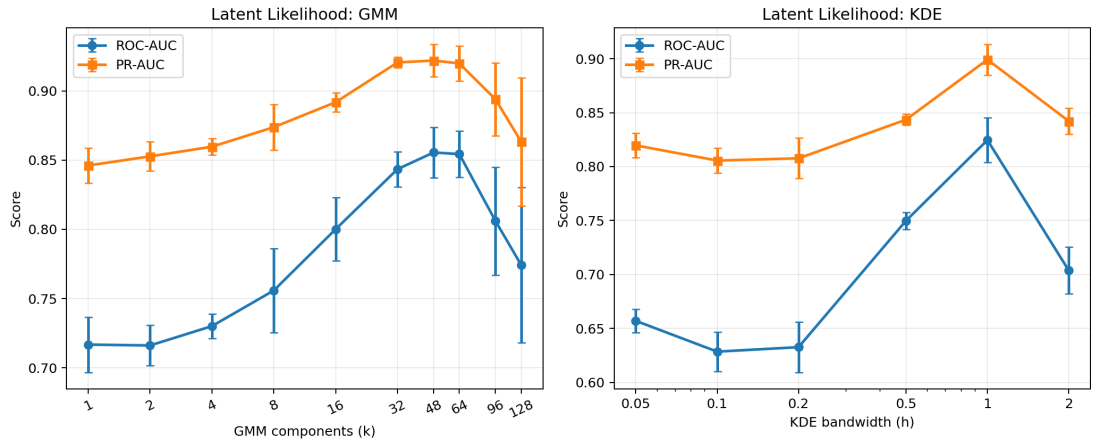


**Figure 2.** Latent-likelihood ablation. Left: ROC-AUC and PR-AUC versus GMM component count. Right: ROC-AUC and PR-AUC versus KDE bandwidth (log-scaled). Values are mean  $\pm$  std across three seeds.

### 5.4 Robustness and Statistical Validation

The central result is the seed-robust improvement of latent likelihood scoring over the geometry baseline. With fixed configuration across seeds (GMM(48) in latent space), latent likelihood exceeds AE+manifold ROC-AUC in all three seeds (Table 4), with mean paired gains of +0.0892 ROC-AUC and +0.0552 PR-AUC.

Fusion remains directionally consistent but smaller in magnitude: at fixed  $\lambda = 0.2$ , the mean paired gain is +0.0025 ROC-AUC and +0.0050 PR-AUC. The morphology+latent likelihood variant (fixed KDE bandwidth  $h = 1.0$ ) also improves over baseline (+0.0370 ROC-AUC, +0.0169 PR-AUC) but does not match latent-only likelihood in aggregate.

The morph-only kNN result is included for completeness; under the fixed-data protocol it is deterministic, so repeated seed entries are identical by construction.

For transparency, single-run curves in Figure 1 are illustrative; headline claims are based on the 3-seed aggregates in Tables 2 and 4.

**Table 4.** Paired seed-wise metric deltas relative to the AE+Manifold baseline ( $\alpha = 0.5, \beta = 2.0$ ) under fixed-config reporting. Values are mean  $\pm$  std across seeds 101/202/303. “Wins (AUC)” counts seeds where the method’s ROC-AUC exceeds baseline.

Comparison	$\Delta$ ROC-AUC	$\Delta$ PR-AUC	Wins (AUC)
Fusion ( $\lambda = 0.2$ )	$+0.0025 \pm 0.0031$	$+0.0050 \pm 0.0033$	3/3
Likelihood (Latent, GMM(48))	<b><math>+0.0892 \pm 0.0293</math></b>	<b><math>+0.0552 \pm 0.0145</math></b>	<b>3/3</b>
Likelihood (Morph+Latent, KDE( $h = 1.0$ ))	$+0.0370 \pm 0.0312$	$+0.0169 \pm 0.0176$	3/3

## 6 Discussion

The main technical result is straightforward: in this benchmark, latent likelihood scoring is stronger than distance-based geometry scoring. That result is not subtle in Table 2. The gain is large enough to survive seed variation, and it appears in both ROC-AUC and PR-AUC.

Why this likely happens is also fairly clear from the behavior we saw during tuning. The geometry score improved as manifold weight increased, then plateaued. That pattern suggests the latent space does contain useful separation structure, but local distance alone does not use all of it. A likelihood model can use global shape in the latent distribution, including multi-modal structure, rather than only nearest-neighbor deviation. In a confusion-limited mixture, that extra distributional information matters.

The fusion result is useful but modest. Adding morphology features helped in direction, but the effect size was small relative to likelihood in latent space. That does not mean morphology is irrelevant. It means that, with the current feature design and weighting, morphology behaves more like a secondary cue than a dominant discriminator.

The contrastive branch is a negative result worth keeping in the record. Training dynamics changed, but ranking performance did not reliably improve. For this problem, stronger invariance pressure did not automatically produce a better one-class geometry. That is an important practical point, especially for readers who might expect contrastive losses to dominate by default.

There are also limits we should state plainly. The benchmark is synthetic and controlled by construction. That is appropriate for method comparison, but it is not the same as full mission realism. Also, precision and recall in this paper come from a fixed median-score operating rule, so they are protocol diagnostics rather than operating-point claims for deployment. Finally, while we moved to fixed-config reporting in the main comparisons, the overall method-development process still involved iterative exploration; that should be kept in mind when interpreting effect sizes.

Taken together, the evidence supports a specific conclusion for this setting: once a stable CWT representation is in place, changing the one-class scoring rule can matter more than incremental tuning of geometry weights.

## 7 Conclusion and Future Work

This paper compared one-class scoring strategies for resolvable-source ranking in confusion-limited synthetic LISA data under a fixed data and preprocessing protocol. The strongest performer was likelihood-based scoring in latent space, with consistent gains over the AE+manifold baseline across all three seeds. Morphology fusion improved baseline performance, but with smaller effect size, and the contrastive geometry branch did not yield reliable gains in this setup.

The next step is to test whether this advantage survives controlled distribution shift rather than only one benchmark regime. A direct follow-up is to evaluate the same fixed methods under at least three shift axes: confusion level (e.g.,  $N_c = 500, 1000, 2000$ ), source-mixture shift (e.g., MBHB/EMRI/GB ratios), and resolvable-source SNR range shift. We would treat robustness as the primary endpoint and report both mean AUC/AP and degradation relative to the in-distribution baseline for each axis.

A second follow-up is to replace the median-score operating-point diagnostic with an explicit false-alarm-constrained threshold policy. Concretely, thresholds can be calibrated on background-only validation segments to target fixed FPR levels (for example  $10^{-1}$ ,  $10^{-2}$ , and  $10^{-3}$ ), then evaluated on held-out test sets for recall and precision at each operating point. This would translate the ranking result into deployment-relevant operating behavior.

Finally, if latent likelihood remains superior under those tests, model complexity should be increased only under the same fixed-protocol discipline used here. The criterion for adopting more expressive density models should be consistent, seed-robust gains over the current GMM/KDE baselines under both in-distribution and shifted conditions, rather than isolated single-run improvements.

### Code and Data Availability

To ensure reproducibility, all experiments reported in this paper are tied to the public repository <https://github.com/jericho-cain/lisa-cwt-oneclass-likelihood> at tag v1.0.0-paper; the repository includes fixed seed configurations, evaluation scripts, and the figure/table summary artifacts used in the manuscript.

### References

- [1] Nelemans G, Yungelson L R and Portegies Zwart S F 2001 *Astronomy & Astrophysics* **375** 890–898 ISSN 1432-0746
- [2] Timpano S E, Rubbo L J and Cornish N J 2006 *Physical Review D* **73** 122001 ISSN 1550-2368
- [3] Crowder J and Cornish N J 2007 *Physical Review D* **75** 043008 ISSN 1550-2368
- [4] Robson T, Cornish N J and Liu C 2019 *Classical and Quantum Gravity* **36** 105011 ISSN 1361-6382
- [5] LISA Consortium 2018 Lisa science requirements document Tech. Rep. ESA-L3-EST-SCI-RS-001 European Space Agency
- [6] Owen B J 1996 *Physical Review D* **53** 6749–6761 ISSN 1089-4918
- [7] Chatterji S, Blackburn L, Martin G and Katsavounidis E 2004 *Classical and Quantum Gravity* **21** S1809–S1818 ISSN 1361-6382
- [8] Klimenko S, Yakushin I, Mercer A and Mitselmakher G 2008 *Classical and Quantum Gravity* **25** 114029 ISSN 1361-6382
- [9] LISA Collaboration 2017 Laser interferometer space antenna (*Preprint* [1702.00786](#))
- [10] Cornish N and Robson T 2017 *Journal of Physics: Conference Series* **840** 012024 ISSN 1742-6596 (*Preprint* [1703.09858](#))
- [11] Gabbard H, Williams M, Hayes F and Messenger C 2018 *Physical Review Letters* **120** 141103 ISSN 1079-7114
- [12] George D and Huerta E 2018 *Physics Letters B* **778** 64–70 ISSN 0370-2693
- [13] Powell J, Trifirò D, Cuoco E, Heng I S and Cavaglià M 2015 *Classical and Quantum Gravity* **32** 215012 ISSN 1361-6382
- [14] Moreno E A, Borzyszkowski B, Pierini M, Vlimant J R and Spiropulu M 2022 *Machine Learning: Science and Technology* **3** 025001 ISSN 2632-2153
- [15] Fayad A 2024 Unsupervised learning approach to anomaly detection in gravitational wave data (*Preprint* [2411.19450](#))
- [16] Cain J E 2026 *Classical and Quantum Gravity* ISSN 1361-6382
- [17] Cain J 2025 Manifold learning for source separation in confusion-limited gravitational-wave data
- [18] Schölkopf B, Platt J C, Shawe-Taylor J, Smola A J and Williamson R C 2001 *Neural Computation* **13** 1443–1471 ISSN 1530-888X
- [19] Dempster A P, Laird N M and Rubin D B 1977 *Journal of the Royal Statistical Society Series B: Statistical Methodology* **39** 1–22 ISSN 1467-9868
- [20] Parzen E 1962 *The Annals of Mathematical Statistics* **33** 1065–1076 ISSN 0003-4851